Engineering Structures 306 (2024) 117739

Contents lists available at ScienceDirect

Engineering Structures

journal homepage: www.elsevier.com/locate/engstruct

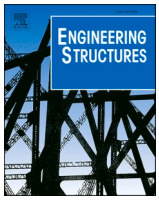

Structural design of reinforced earthcrete (ReC) beams

M. Franciosi [a], V. Savino [a], L. Lanzoni [b,*], A.M. Tarantino [b], M. Viviani [a]

[a] HEIG-VD/HES-SO - Haute Ecole d'Ingénierie et de Gestion du Canton de Vaud, Route de Cheseaux 1, CH-1401 Yverdon, Switzerland
[b] Department of Engineering "Enzo Ferrari", University of Modena and Reggio Emilia, 41125 Modena, Italy

ARTICLE INFO

Keywords:
Flexural behavior
Earthen materials
Eco-building construction
Four point testing
Adherence strength

ABSTRACT

This paper presents the results of an extensive experimental campaign aimed at evaluating the feasibility of using steel-reinforced earthen materials for load-bearing structural applications, with a focus on a new category termed "shot-earth". Addressing excavated soil, a major source of construction waste, shot-earth demonstrates remarkable properties, such as notable green strength and reduced water sensitivity. The experimental program includes four-point bending tests on steel-reinforced shot-earth beams, along with pull-out tests to assess the adherence between ribbed steel bars and shot-earth. A flexural design approach, traditionally suited for reinforced concrete, is presented and validated to establish a reliable model for reinforced shot-earth elements in bending state. These findings suggest that leveraging existing models for reinforced concrete can overcome some traditional challenges associated with earth-based constructions, promoting them as a viable and ecological alternative to conventional construction materials.

1. Introduction

Earthen construction has stood the test of time, serving as a fundamental resource for building projects around the world for centuries. Its enduring appeal among the scientific community stems from its unique attributes that combine sustainability with utility [1]. Three notable advantages of utilizing earth building materials are: (i) Their potential to reduce CO2 emissions, given that even when stabilized, earthen constructions contain a lower amount of cement compared to other materials [2,3]. (ii) The cost-saving benefits arising from the direct use of excavated soil in the field. (iii) The natural aesthetic value they confer [1,4]. Currently, the predominant methods of earth-based construction — suitable for the erection of single or two-story civil buildings — involve the use of adobe, cob, and rammed-earth techniques [1,4].

Recently, a soil-based construction material known as "shot-earth" (hereafter referred to as "SE") has been introduced to the global scientific community, with studies undertaken to analyze its mechanical, thermal, and hygrothermal properties [5–10]. SE represents a new category of sustainable construction materials composed of excavated soil, aggregates, and a small amount of stabilizer, if dictated by performance requirements. To minimize the depletion of natural resources, the utilization of recycled aggregates is preferred in the manufacturing of SE. Stabilization can be achieved not only through the addition of cement but also by incorporating agents with a lower carbon footprint, such as lime, hydraulic lime, and plaster. The mixture of raw materials undergoes a high-speed projection process allowing for the spraying of SE into formworks, which ensures a high degree of compaction. This fabrication process, rooted in shotcrete technology, imbues SE with green strength. Following a standard 28-day curing period, SE attains a compressive strength exceeding 9 MPa [5].

The interest in SE is steadily growing, driven by compelling research that not only showcases its potential applications but also elucidates its limitations, offering clear guidelines to architects, engineers, contractors, and building owners.

Often, classic earthen materials still face significant challenges in being accepted as structural materials [11] due to prejudices related to: (i) low compressive strength, albeit it can exceed 5 MPa when stabilized with cement [12,13]; (ii) water sensitivity; (iii) high maintenance requirements; and (iv) the absence of predictive models to accurately calculate and detail structural members. These prejudices can be overcome through innovation and research. To equip structural designers with the tools necessary to build safely with SE, numerous research studies have been undertaken. This paper presents the study and validation of a mechanical model devised to forecast the flexural response of reinforced SE beams. This model builds upon those established for concrete structures. Capitalizing on the existent knowledge of RC, the model modifies and tailors it to accommodate the distinct characteristics of earthen materials reinforced with steel. This approach paves the way for designs that are both reliable and sustainable in the construction of

* Corresponding author.
E-mail address: luca.lanzoni@unimo.it (L. Lanzoni).

https://doi.org/10.1016/j.engstruct.2024.117739
Received 24 September 2023; Received in revised form 22 January 2024; Accepted 20 February 2024
Available online 6 March 2024

Nomenclature

SE	Shot-earth.
RC	Reinforced concrete.
SE772	SE mix design composed by 7 parts of soil, 7 parts of aggregates and 2 parts of cement by weight.
SE772 *	SE mix design with the same proportion of SE772 but with the use of a different streak of earth.
B_SE772	SE772 beams for the four-point bending test.
P_SE772 * _l_ ø	SE772 * prisms for the pull-out test with an embedding length "l" and a rebar diameter "ø".
SE772 * _C-28	Cubic samples for SE772 * characterization in terms of C-28 and BD.
C-28	28-days compressive strength.
BD	Bulk density.
EM	Elastic modulus.
EM_{SE}	SE Elastic modulus.
EM_{SE772}	SE772 Elastic modulus.
χ	Curvature.
M_a	Bending moment for a defined cross section corresponding to a specific value of χ.
M_0	Midspan moment due to the self-weight load of the reinforced B_SE772.
J	Inertia modulus of the cross section.
J_{om}	Inertia modulus of the homogenized cross section.
δ	Midspan displacement.
P	Total load applied during the four-point bending test.
P_1	Load applied by the first servo-hydraulic actuator in the four-point bending test.
P_2	Load applied by the second servo-hydraulic actuator in the four-point bending test.
P_{min}	Minimum load applied in phase S1.
P_{max}	Maximum load applied in phase S1.
P_u	Maximum load recorded during the four-point bending test.
M_u	Maximum bending moment recorded during the four-point bending test.
$\delta(M_u)$	Midspan displacement at M_u.
$M^R(z_1)$	Bending moment for the real frame B_SE772 in the variable z_1.
$M^f(z_1)$	Bending moment for the fictional frame B_SE772 in the variable z_1.
$M^R(z_2)$	Bending moment for the real frame B_SE772 in the variable z_2.
$M^f(z_2)$	Bending moment for the fictional frame B_SE772 in the variable z_2.
S1	First loading step in the four-point bending test configuration.
S2	Second loading step in the four-point bending test configuration.
δ_{int}	Intrados displacement measured by horizontal LVDTs glued on the bottom fiber during the S1.
δ_{ext}	Extrados displacement measured by horizontal LVDTs glued on the top fiber during the S1.
LVDT	Linear Variable Displacement Transducer.
l_{cr}	LVDT characteristic length.
h	B_SE772 cross section height.
L	B_SE772 span length.
τ	Bond stress.
τ_{max}	Average bond stress from experimental results.
$\tau_{max,CEB}$	Average bond stress from concrete predicted model.
s	Slip.
$F_{P\_SE772^*,max}$	Pull out force.
ø	Rebar diameter.
l	Embedded length.
f_{cm}	Mean cylinder compressive strength.
C_{min}	Minimum cover thickness.
C_{max}	Maximum cover thickness.
K_{tr}	Efficiency of the confinement coefficient.

earthen structures.

This paper presents experimental results to validate the proposed model. Within the structural investigation, three reinforced SE beams (labeled hereafter "B_SE772") are analyzed.

The bond between concrete and steel rebars is a pivotal factor in determining the flexural performance of reinforced concrete members [14]. Accordingly, to scrutinize the bond behavior between SE772 and steel bars, six pull-out tests were conducted. Subsequently, a critical comparison was undertaken involving the bond stress–slip relationship delineated in the CEB-FIP model code 90 [15] and the CEB-FIP model code 2010 [16]. The bond behavior can also be influenced by the coefficient of thermal expansion between materials. As the constituent materials used in the production of shot-earth are the same as those employed in general earth-based materials, the conclusions drawn for rammed Earth and Compressed Stabilized Earth Block materials can be extrapolated to shot-earth, specifically the identical coefficient of thermal expansion between steel and shot-earth, as stated in [17,18].

2. Materials and methods

2.1. Materials and mixture proportions

SE represents a novel class of sustainable construction materials composed of excavated soil, aggregate (sized 0–8), stabilizing agents, and water. In the experiments, the mix proportion designated as SE772 (mix proportion by mass: 7 parts of soil, 7 parts of aggregates, and 2 parts of cement) was employed for four-point loading bending test of the reinforced SE beams. The same mix proportion was exploited for the pull-out tests. However, it is worth noting that two distinct types of soil were used for each test. As a result, the mix used in the pull-out tests will be subsequently referred to as SE772 * . The purpose of the pull-out tests is to assess, for a generic SE772 recipe, whether the assumption of perfect adhesion proves to be valid, assuming that minor variations in the composition of the earth do not affect the bonding behavior. In order to characterize the soils, a particle size analysis was conducted to assess its granulometric distribution according to the EN 933–1 standard [19], see Fig. 1. Additionally, the USCS classification was established [20], leading to the conclusion that SE772 can be grouped into CL-ML, while SE772 * falls into the CL category. The extraction of both soils occurred at a depth greater than 60 cm to avoid the presence of organic material.

The water content in the mix stands at 8.66% of the dry mixture's mass, as detailed in [6]. The application of SE involves a high-speed (300 km/h) dry projection process using a specially designed machine. This rapid projection technique endows SE with a notable density (approximately 2100 kg/m^3) and significant green strength immediately post-placement, as it is capable of maintaining its shape inside the formwork without visible deformations and without cracking before reaching its maximum strength. For constructing load-bearing structures, such as beams, SE is reinforced using steel rods compliant with the Swiss standard type B500B. This reinforcement method aligns with the recommendations for concrete beam reinforcement. The same steel rods were also incorporated in the pull-out test specimens.

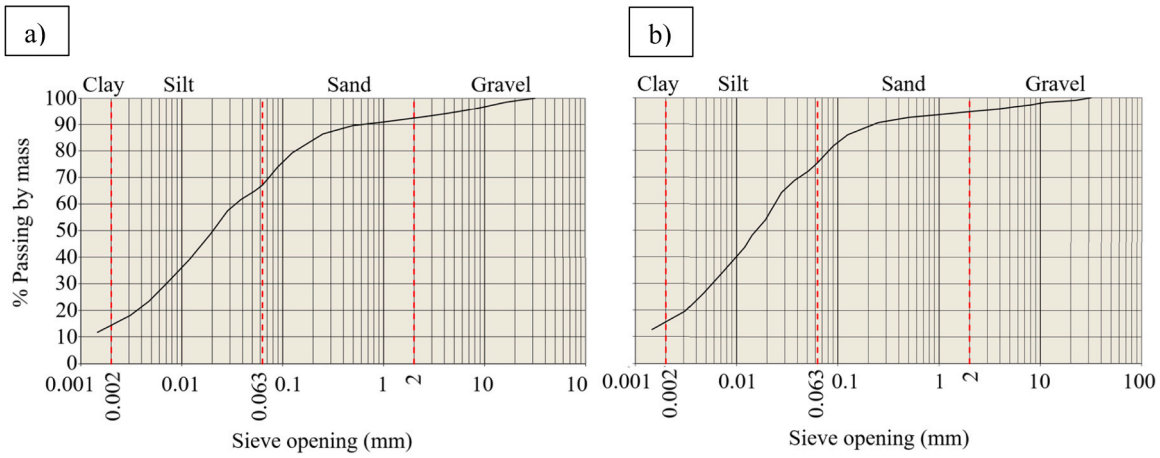

Fig. 1. Granulometric analysis of: a) SE772 soil, b) SE772 *soil.

2.2. Fabrication and curing of test specimens

To perform the four-point loading bending tests, three prismatic samples of length 4000 mm and size 300 × 400 mm^2 were constructed. The geometric features and the layout of the longitudinal and shear steel reinforcements are sketched in Fig. 2.

The mix design used for the SE beams aligns with the methodology employed in [5], ensuring consistent mechanical properties across the samples. Fig. 3 captures the step of projecting SE into the formworks. It is important to highlight that a specific spray angle is necessary to prevent aggregate bounding and to achieve optimal compaction.

Given that perfect adherence between SE and steel rebars cannot be taken for granted, several pull-out tests were conducted. To facilitate this, prismatic SE samples measuring 150 × 150 x 300 mm^3 (hereafter referred to as "P_SE772 *_l_ ø") were crafted. In the P_SE772 * _l_ ø label, l denotes the embedded length, while ø represents the steel rebar diameter (expressed in mm). A different geometry can alter the results in terms of the bond stress-slip relationship, as it can also influence the failure mechanism. The shear bond stress at failure exhibits a decreasing trend with an increase in specimen size. Experimental findings documented in [21] suggest that larger specimens, featuring correspondingly larger bars, are prone to failure in a more brittle, splitting mode. Conversely, smaller bars tend to undergo a less brittle or more plastic shear pullout mode upon failure. This shift in failure modes based on specimen size aligns with the physical implications of the size effect law [22]. For the purpose of the test, it was chosen to have an upper concrete cover greater than 5ø, ensuring a good confinement condition according to [16]. This configuration also aligns to various tests documented in the Literature [23,24]. The bar diameter for all pull-out tests is set at 12 mm, matching the specifications employed in the bending tests conducted on the beams.

Within each sample, a single steel rebar was embedded, as depicted in Fig. 4. These specimens, with varied embedded lengths (10ø and 15ø), were grouped and tested in sets of three for each specified length.

To evaluate the bulk density (subsequently termed "BD") and the 28-day compressive strength (referred to as "C-28") of SE772 * , an additional four cubical specimens with dimensions of 150 × 150 x 150 mm^3 were produced.

All specimens were cast on a single day at a construction site in Moudon, Western Switzerland. After a curing period of 7 days under summertime external conditions, the specimens were transported to the laboratory at Haute Ecole d'Ingénierie et de Gestion du Canton de Vaud (HEIG-VD) to complete the curing (28 days) at T = 23 ± 3 °C and RH = 50 ± 5%. The curing process does not involve immersion in water, as

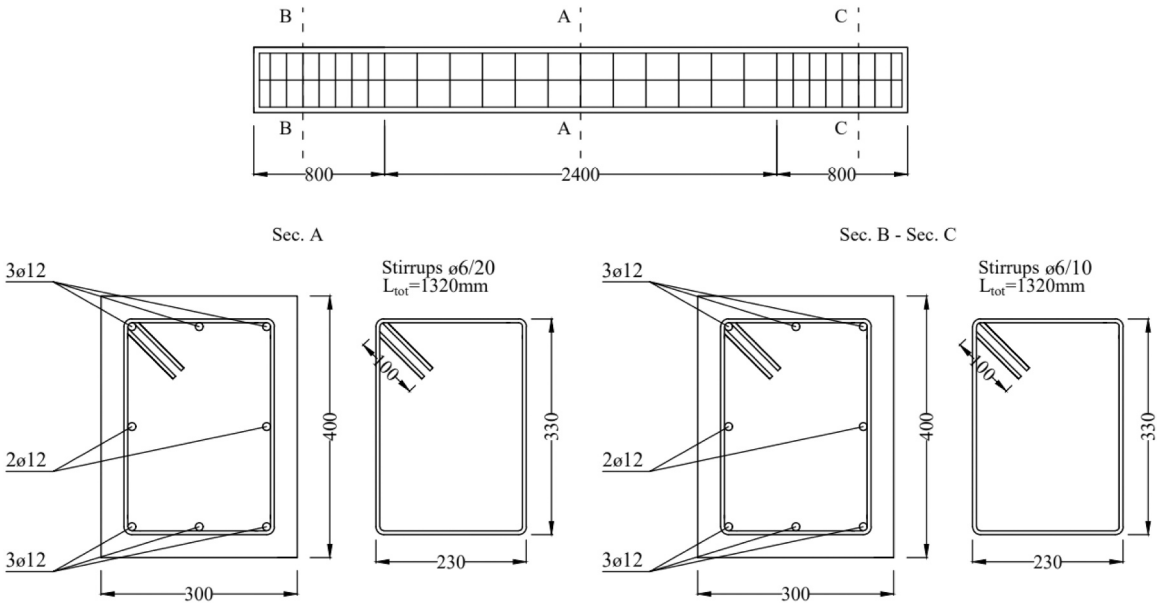

Fig. 2. B_SE772: layout of the longitudinal and shear steel reinforcements.

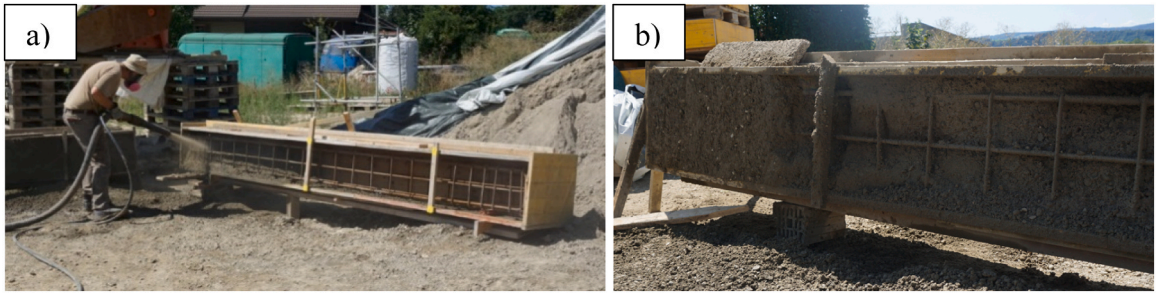

Fig. 3. a) Fabrication of B_SE772, b) B_SE772 realized portion during the projection process.

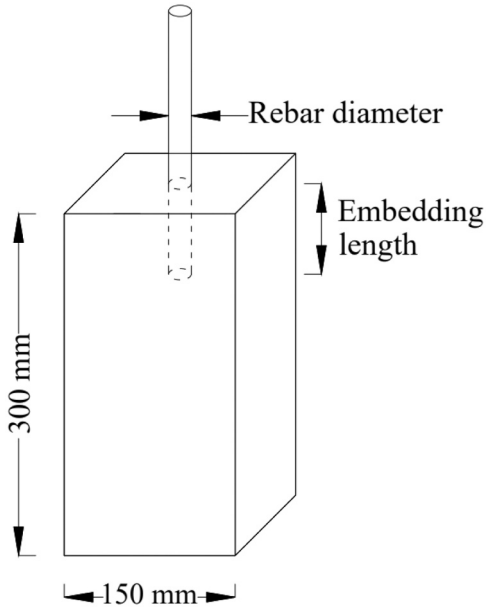

Fig. 4. SE772 sample used to perform the pull-out test.

this could result in strength losses due to the presence of soil in the mix proportion, making it susceptible to water.

An overview of the executed tests and their corresponding standards can be found in Table 1.

2.3. Compressive test

To ascertain the C-28 for the SE772 * mixture, uniaxial unconfined compressive tests were executed in line with the European standard used for concrete materials [26]. These compressive assessments were carried out utilizing a 5000 kN Perrier testing apparatus. The procedure entailed an initial preload of 15 kN, followed by a loading rate of 0.3 MPa/s, consistent with the standards.

Table 1
Experimental tests carried out on specimens.

Specimens	Label	Test	Regulation
SE772 * Prism $0.15 \times 0.15 \times 0.3$ m^3	P_SE772 * _ $l^{(a)}$_ $\varnothing^{(b)}$_i	Pull-out test	[14,25]
SE772 * Cubes $0.15 \times 0.15 \times 0.15$ m^3	SE772 * _C-28_i	Compressive test	[26]
SE772 Beams $0.3 \times 0.4 \times 4$ m^3	B_SE772	Four-point loading bending test	[27–30]

(a): Embedding length (mm)
(b): Steel rebar diameter (mm)
* Different streak of earth used
i: Sample number

2.4. Pull-out test

The bond between steel rebars and SE772 * was assessed using pull-out tests. Each test was conducted by applying a consistent slipping speed of 0.03 mm/s, as cited in [25,31]. The total displacement of the rebar in relation to the SE772 * support was gauged using a specific LVDT sensor setup, as illustrated in Fig. 5. Both the LVDT displacement readings and the pull-out force were captured at a frequency of 10 Hz.

As the stress distribution along the embedded length is not uniform is usual to define an average bond stress as reported in Eq.(1),

$$\tau_{\max} = \frac{F_{P_{SE772*},\max}}{\pi \times \varnothing \times (l - s)} \tag{1}$$

where: $F_{P\_SE772*,max}$ is the pull-out force (N), ϕ is the rebar diameter (mm), l is the embedded length (mm) and s is the slip between the steel bar and the SE772 * (mm).

For monotonic loading conditions, the bond stress can be calculated according to the predictive models as a function of the relative displacement as reported in Eq. (2),

$$\tau = \begin{cases} \tau_{\max}\left(\frac{s}{s_1}\right)^{\alpha} & 0 \le s \le s_1 \\ \tau_{\max} & s_1 < s \le s_2 \\ \tau_{\max} - (\tau_{\max} - \tau_f)\left(\frac{s - s_2}{s_3 - s_2}\right) & s_2 < s \le s_3 \\ \tau_f & s > s_3 \end{cases} \tag{2}$$

where the required parameters are listed in Table 2. It should be noted that these values are valid for: (i) a "good" bond condition, (ii) splitting failure, (iii) ribbed bars in which the tensile strain is lower than its yield limit. Regarding the CEB-FIP MC2010 model, the $\tau_{\max}$ value takes into account the confinement effect provided both by the concrete and the stirrups as reported in Eq. (3),

$$\tau_{u,split} = 7 \times \left(\frac{f_{cm}}{20}\right)^{0.25} \tag{3}$$

where f_{cm} is the mean cylinder compressive strength evaluated as 83% of the cubic one (MPa).

2.5. Four point loading bending test

2.5.1. Experimental setup

The beams were supported on a roller and a spin support, with a span length equal to 3810 mm (labeled hereafter "L"). A load frame was assembled and equipped with two 300 kN servo-hydraulic actuators intended to apply two pointwise loads to the beam in accordance with the four-point loading bending test setup, see Fig. 6(a).

The load was applied by a deflection rate of 2 mm/min [27–30]. A displacement sensor was connected to the piston that was loaded with "P_2" (see Fig. 6(a)) to define the correct testing speed. The pistons were connected to the same oil circuit, ensuring uniform force values

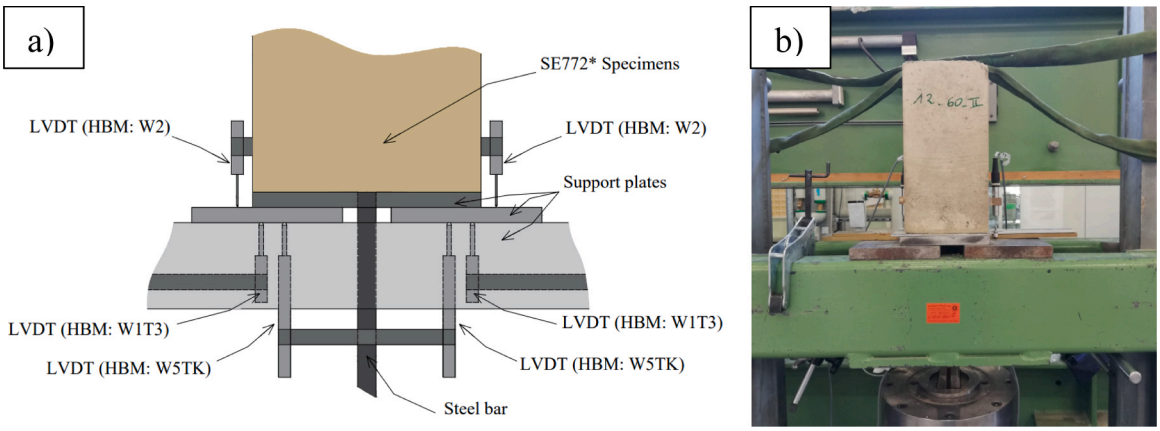

Fig. 5. a) Detail of LVDTs arrangement setup, b) Pull-out experimental setup.

Table 2
Parameters involved in the bond stress-slip relationship.

	CEB-FIP MC90	CEB-FIP MC2010
s_1	0.6 mm	$s(\tau_{u,split})$
s_2	0.6 mm	s_1
s_3	1.0 mm	1.2 s_1
α	0.4	0.4
τ_{max}	$2\sqrt{fcm}$	$\tau_{u,split}$ (Eq.(3))
τ_f	0.15 τ_{max}	0

throughout the test. A monitoring was conducted during the test to verify compliance, as both pistons were connected to force sensors. Notably, the maximum difference recorded at the point of failure, with regard to the force measured on the two pistons was less than 0.9%.

The four-point loading bending test was conducted in two distinct loading phases. The first loading step (S1) includes 3 cycles of loading-unloading performed in the elastic regime of the beam. For all 3 cycles, the minimum (P_{min}) and maximum (P_{max}) load values are 8–10 kN and 30–40 kN, respectively. S1 is requested to first simulate the mechanical response under operational loads and second to validate the loading and the support setup. In the following, the total load (P) acting on the beams is considered as the sum of two equal forces effectively applied to the beams (P_1 and P_2), see Fig. 6(a). The second loading step (S2) begins as soon as the first one is finished. S2 permits to characterize the mechanical response of the beam by applying a total load starting from P_{min} which gradually increases until to reach the total failure. As showed in Fig. 6(b), a LVDT system is fixed on the skin of the beam to measure the stretch and the midspan deflection. Specifically, four LVDTs are utilized, with two allocated to each side of the beam: one placed horizontally on the top fiber and one on the bottom fiber. An additional four LVDTs are positioned vertically on the beam: one on the extrados, one in the middle of each side, and one on the intrados fibers. Data from these LVDTs are continuously recorded using a digital acquisition system at a frequency of 10 Hz.

2.5.2. Modeling

To establish the relationship between moment and midspan deflection, a suitable model for RC is proposed in this study. The stress-strain relationships considered here involve the classical parabolic-rectangular curve with an ultimate compressive strain of 3‰ [32] for the SE. The adoption of a constitutive model typically used for concrete is supported by analyses of the mechanical properties of SE conducted in [5]. Further details regarding the stress-deformation behavior under compression are reported in [9].

Meanwhile, for the B500B steel, an elastic-plastic relationship is used, which accounts for strain hardening up to 5% of the ultimate strain. As the curvature, denoted as χ, increases, the corresponding moment, denoted as M_a, is evaluated up to the point of failure. Failure is determined either when the SE undergoes compression or when the steel bars experience traction failure. The foundational assumptions guiding this process include: (i) plane cross sections remaining plane even after deformation, and (ii) perfect adhesion between the steel reinforcement and SE, a finding supported by results presented in Section 3.2. To calibrate the model, reference was made to the mechanical properties outlined in [5].

Through the function that best approximates the χ-M_a relationship (see Fig. 7), it is possible to determine the moment of inertia J of the cross section as a function of M_a, as reported in Eq. (4),

$$J = \frac{M_a}{EM_{SE} \times \chi(M_a)} \tag{4}$$

where M_a is the bending moment (Nmm), EM_{SE} is the SE772 elastic modulus (MPa) and $\chi(M_a)$ is the curvature at a specific value of M_a (mm^{-}

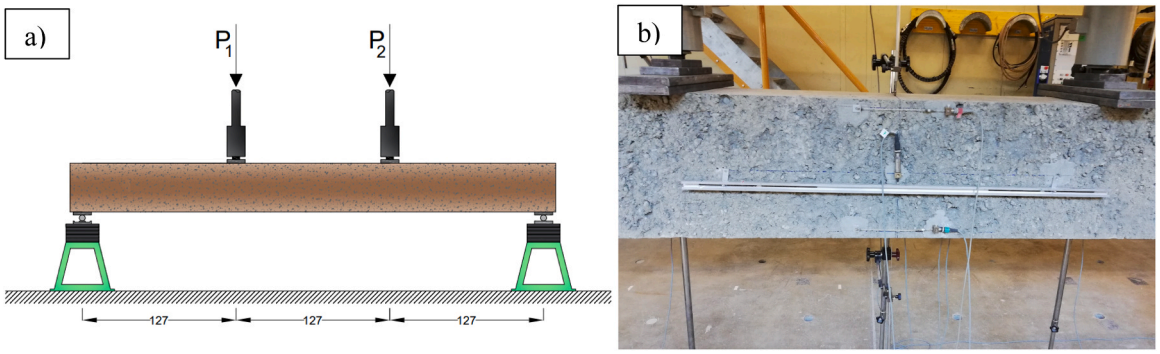

Fig. 6. a) Load pattern for four-point loading bending test b) LVDT's arrangement.

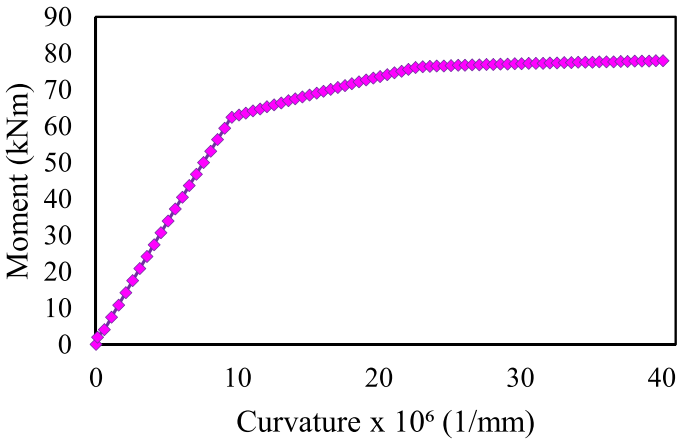

Fig. 7. M_a-χ relationship.

[1]).

The determination of the midspan displacement as a function of M_a was subsequently obtained using the principle of virtual work. As reference of the real and fictional schemes, the Eqs. (5) and (6) can be drawn,

$$M^R(z_1) = F\,z_1\,,\; M^f(z_1) = \frac{1}{2} \quad z_1, 0 \le z_1 < \frac{L}{3} \tag{5}$$

$$M^R(z_2) = \frac{F}{3}\frac{L}{3},\; M^f(z_2) = \frac{L}{6} + \frac{z_2}{2} \quad 0 \le z_2 \le \frac{L}{6} \tag{6}$$

and the δ determined as reported in Eq. (7),

$$\delta = 2\left(\int_0^{\frac{L}{3}} \frac{M^f(z_1)}{EM_{SE772}}\frac{M^R(z_1)}{J\left(M^R(z_1)\right)}dz_1 + \int_0^{\frac{L}{6}} \frac{M^f(z_2)}{EM_{SE772}}\frac{M^R(z_2)}{J\left(M^R(z_2)\right)}dz_2\right) \tag{7}$$

where: δ is the midspan deflection for B_SE772, $M^R(z_1)$ and $M^R(z_2)$ are the bending moments due to the real loading, $M^f(z_1)$ and $M^f(z_2)$ are the bending moments due to the virtual unitary loading, L is the effective beam length and $J(M^R(z_1))$ is the moment of inertia as a function of the bending moment due to the real moment. Shear contributions have been neglected.

3. Results and discussion

3.1. Compressive test

The crack pattern observed in the SE772_C-28 is deemed satisfactory per the criteria laid out in standard [26], as illustrated in Fig. 8. Table 3 presents a summary of the engineering properties of SE772 * , derived from the tests conducted on the cubic specimens. The obtained standard deviation aligns with results from compression tests on earth-based materials [5,6,33].

Table 3
Engineering properties of SE772 * .

Specimens	BD (kg/m^3)	C-28 (MPa)
SE772_C-28_1	2107.20	14.38
SE772_C-28_2	2084.83	13.62
SE772_C-28_3	2071.61	12.84
SE772_C-28_4	2048.89	10.04
Avg.±Std Dev.	**2078.13±24.41**	**12.72±1.89**

C-28: 28-day compressive strength value
BD: Bulk density after curing

3.2. Pull-out test

Despite the confinement offered by the SE cover at a minimum thickness of 12ø, all of the P_SE772 * _l_ ø specimens failed by splitting, as shown in Fig. 9. This is mainly due to: (i) the insufficient confinement provided by the SE, and (ii) absence of stirrups.

In Fig. 10, a comparison between the experimental results and the CEB-FIP MC90 [15] and CEB-FIP MC2010 [16] predictive models is presented in terms of bond stress-*vs*-slip relation.

In Fig. 10, the initial curved segment derived from the models corresponds to the phase where the ribs penetrate the mortar matrix, a process accompanied by micro-cracking. Experimental outcomes for this initial segment align well with model predictions, irrespective of the embedding length. Upon reaching τ_{max}, the declining phase begins, attributed to the splitting failure evident in these results.

Table 4 details a comparison between the τ_{max} observed for each specimen and the values predicted by the two models. For an embedding length of 10ø, τ_{max} shows a significant alignment with $\tau_{max,CEB\text{-}MC2010}$; the relative error for each specimen remains under 17%. Conversely, P_SE772 * _15ø _12 typically registers values higher than those anticipated by the models. Yet, a consistent pattern emerges, demonstrating that τ_{max} augments in tandem with the bonded length. As such, for embedding lengths exceeding 10ø, there is a pronounced alignment with the predictive model tailored for RC materials under optimal bond conditions. This suggests that presuming perfect adhesion between steel bars and SE is a plausible approximation—mirroring assumptions in traditional RC—given a sufficiently long bonded segment.

While the experimental bond stress at a 6 mm slip closely mirrors the standard proposed by CEB-MC90, the declining segment presents a gentler gradient in comparison to anticipated trajectories. This discrepancy may stem from residual bond stresses caused by concrete shearing between ribs. Future investigations are slated to offer a more in-depth characterization of the interplay between SE and steel rebars.

3.3. Four-point loading bending test

In Scenario S1, the horizontal LVDTs, which are affixed to the middle region of the beam, allow for the approximation of the theoretical cur-

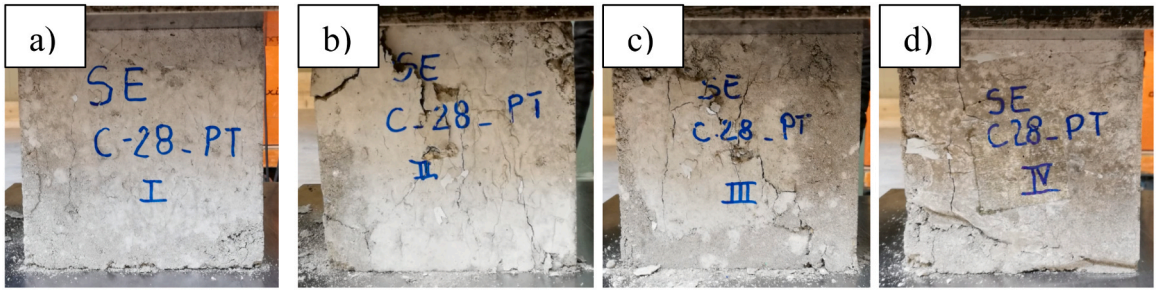

Fig. 8. Crack patterns of: a) SE772 * _C-28_1, b) SE772 * _C-28_2, c) SE772 * _C-28_3, d) SE772 * _C-28_4.

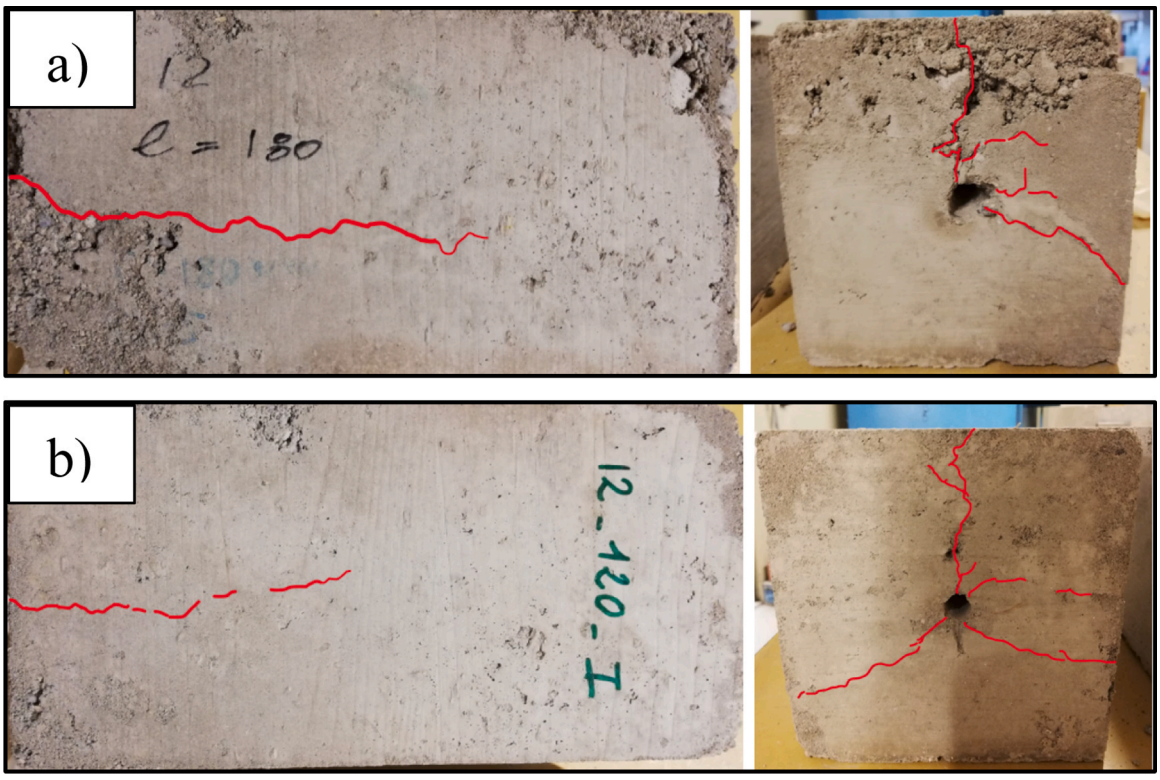

Fig. 9. Splitting failure mode for: a) P_SE772 * _10ø_12, b) P_SE772 * _15ø_12.

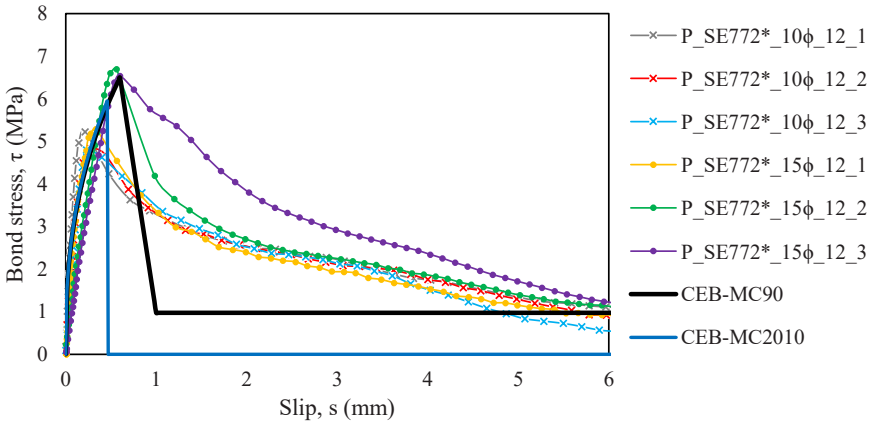

Fig. 10. Bond stress – slip relationship: comparison between experimental results and predictive models.

Table 4
Comparison between experimental and predictive models in terms of τ_{max}.

Specimens	τ_{max} (MPa)	$\tau_{max}/\tau_{max,CEB\text{-}MC90}$ (MPa)	$\tau_{max}/\tau_{max,CEB\text{-}MC2010}$ (MPa)
P_SE772 * _10ø_12_1	5.27	0.81	0.88
P_SE772 * _10ø_12_2	4.95	0.76	0.83
P_SE772 * _10ø_12_3	4.92	0.76	0.83
P_SE772 * _15ø_12_1	5.36	0.82	0.90
P_SE772 * _15ø_12_2	6.75	1.03	1.13
P_SE772 * _15ø_12_3	6.55	1.01	1.10

vature of the cross-section during loading and unloading cycles, see Eq. (8),

$$\chi = \frac{M_0}{EM_{SE772}\ J_{om}} + (\delta_{int} + \delta_{ext})\frac{1}{l_{cr}}\frac{1}{h} \tag{8}$$

where: M_0 is the midspan moment due to the self-weight load of the reinforced B_SE772, EM_{SE772} is the elastic modulus of the SE772 which is assumed as reported in [5], J_{om} is the moment of inertia of the homogenized cross section, δ_{int} is the extension at the intrados measured by horizontal LVDTs glued on the bottom fiber during the S1, δ_{ext} is the shortening at the extrados measured by horizontal LVDTs glued on the top fiber during the S1, l_{cr} is the characteristic length of the LVDT, and h is the height of the beam cross-section.

The Fig. 11 shows the total load applied to the beam (P1 + P2) *vs* the midspan deflection. The self-weight deflection contribution ($\delta = 0.93$ mm), computed according to the theory of elasticity, has been added to the measured midspan displacement. Furthermore, in Fig. 11 (a) is highlight a comparison between the experimental moment-curvature diagram and the M_a - χ relationship as defined in the model presented in Section 2.5.2. This comparison is intended to validate the theoretical diagram of Fig. 7 in the elastic field.

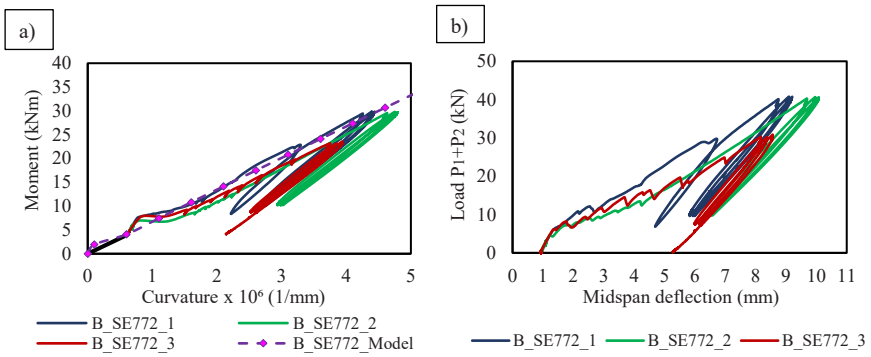

Fig. 11. a) Moment-Curvature diagram in S1 b) Load-midspan deflection diagram in S1.

At the end of S1, the S2 is set to measure the mechanical response of the beam as the load increases until to reach the complete failure, see Fig. 12. The self-weight offset has been considered in S2 too.

All beams in both phases (S1 and S2) display consistent trends, thereby validating the repeatability of the SE manufacturing process. Following the elastic phase, the reinforced SE beams demonstrates ductile behavior, attributable to the presence of the steel reinforcement. Notably, there's a distinct phase where the midspan deflection amplifies while the force remains constant. This behavior closely aligns with that observed in RC beams. The flexural performance metrics for the reinforced SE beams can be found summarized in Table 5.

For all beam samples, the first macro-cracks appear upon reaching the peak load in the midspan. All the samples display similar crack patterns. As seen in reinforced concrete beams, there is an almost homogeneous distribution of vertical cracks corresponding to the position of the steel stirrups embedded in the beam, as shown in Fig. 13. As the load increases, the cracks gradually widen and increase particularly in the neighboring of the supports. At the failure load, the cracks in the central region have an average length of 32 mm and a width of 2 $\pm$ 1 mm, while the cracks in proximity to the supports are characterized by an average length of 20 mm and a width of 0.2 $\pm$ 0.1 mm.

All the reinforced SE beams exhibited failure in a flexural mode. Initially, the steel bars in the bottom fiber undergo plasticization, a phenomenon further corroborated by the plateau observed in Fig. 12. This is followed by a compression failure in the top fiber, as illustrated in Fig. 14(a). The ultimate collapse of the reinforced SE beams arises once the steel bars in the bottom fiber break, as depicted in Fig. 14(b). This highlights a ductile failure, thus confirming the "good bond behavior" [15,16] between SE and steel bars as shown in Section 3.2. This corroborates the assumption of perfect adhesion adopted in Section 2.5.2.

A comparison between the analytical predictions and experimental results in terms of $P_1 + P_2 - \delta$ relationship is shown in Fig. 15. It should be noted that the model well approximates the experimental results in both the elastic and plastic fields. The maximum failure load provided by the model is 123.20 kN with a displacement δ of 50.95 mm. At the theoretical failure point, the SE strain is 3‰, while the steel in the in the lower tension zone reaches 12‰. The differences covered by the experiment are due to a twofold cause: (i) the maximum force of the model is lower due to an additional hardening effect near the failure, (ii) based on the experimentally observed failure domains, it is reasonable to assume the formation of a localized plastic hinge, enabling significant displacements under constant load.

Table 5
Load, Moment and midspan deflection peaks measured during the four-points loading bending test on reinforced SE beams.

Specimens	P_u (kN)	M_u (kNm)	δ (M_u) (mm)
B_SE772_1	139.04	92.08	97.16
B_SE772_2	135.88	90.08	90.92
B_SE772_3	133.80	88.76	85.33
Avg. ±Std Dev	**136.24±2.64**	**90.31±2.64**	**91.14±5.92**

P_u: ultimate load
M_u: ultimate moment
$\delta(M_u)$: Midspan displacement at ultimate moment

4. Conclusions

In this research, an experimental campaign was conducted to characterize the adherence between SE772 and steel bars. Subsequently, the flexural behavior of reinforced SE772 was examined through four-point loading bending tests. Due to the lack of predictive models for earthen structures, existing models designed for RC were employed. These models aimed to predict both the adherence between SE772 and steel bars and the load–displacement relationship of reinforced SE772 members under bending. The presented models were then validated against experimental results. From this research, several conclusions can be drawn:

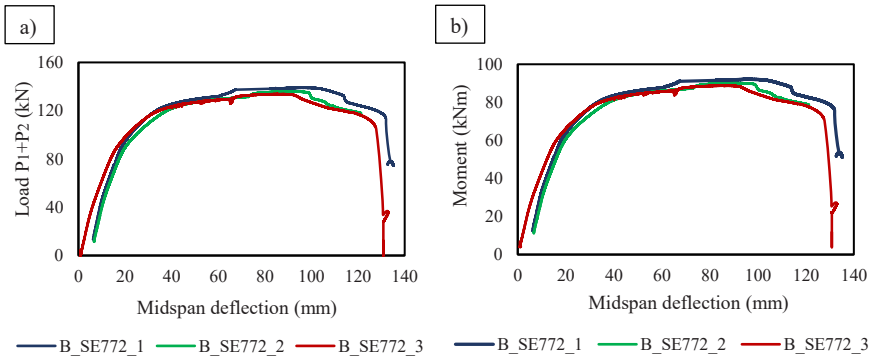

Fig. 12. a) Load-midspan deflection in S2, b) Moment-midspan deflection diagram in S2.

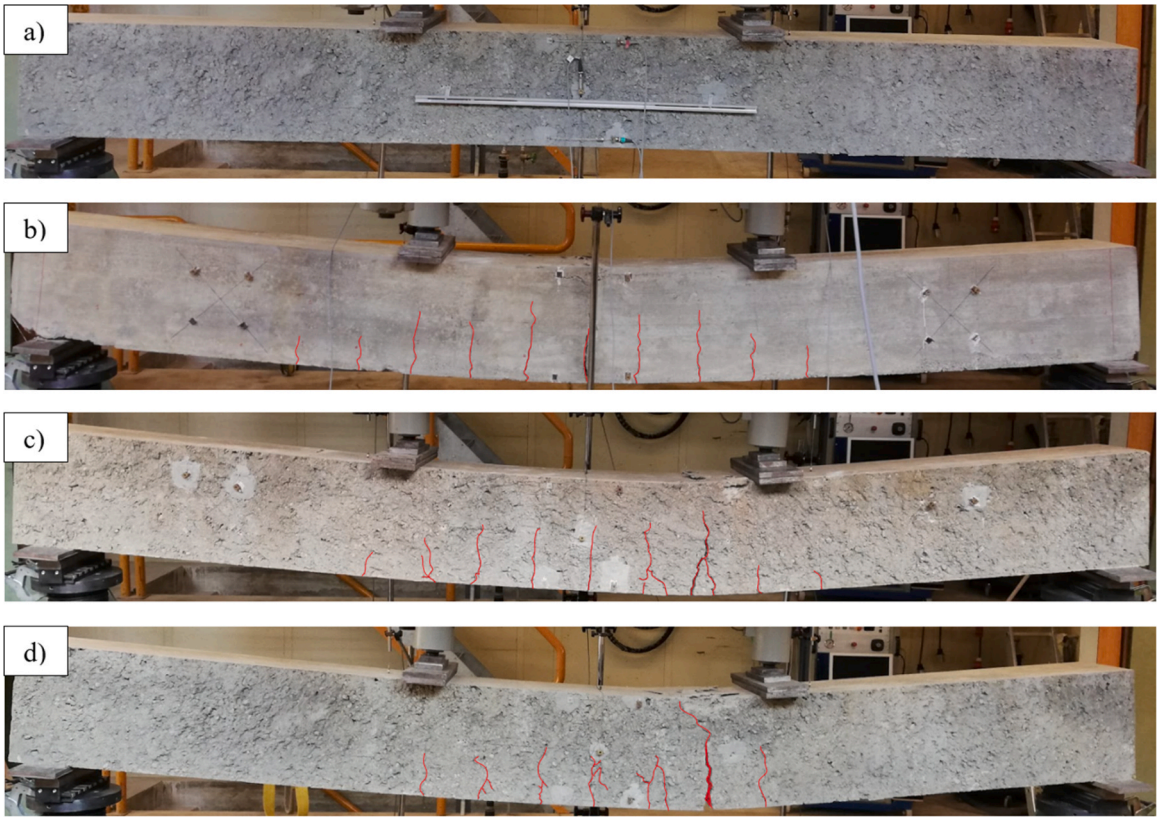

Fig. 13. a) Undeformed configuration. Crack pattern for: b) B_SE772_1, c) B_SE772_2, d) B_SE772_3.

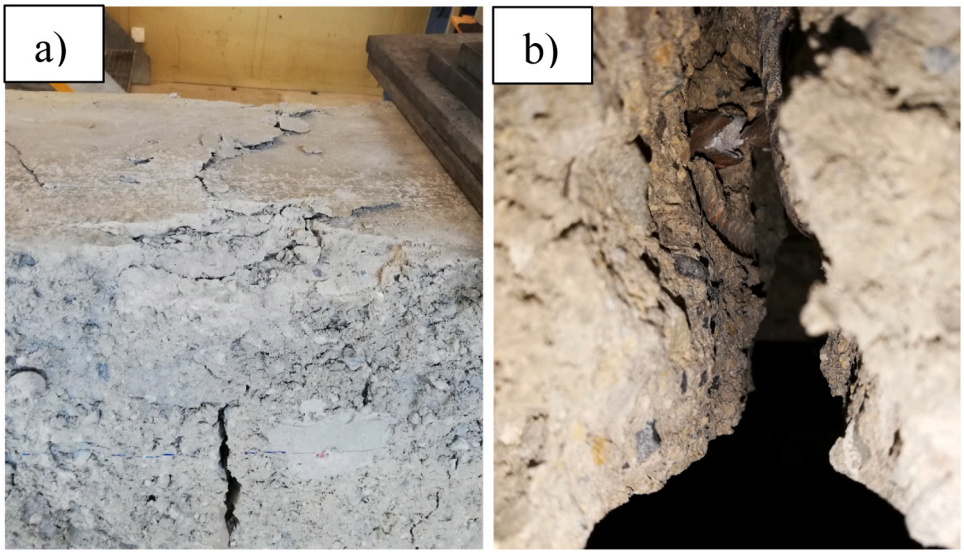

Fig. 14. a) SE failure in compression b) Steel failure.

1. A comparison of suitable predictive models for RC structures with experimental results from pull-out tests supports the hypothesis of perfect adhesion between steel bars and SE materials.
2. The model based on the stress-strain relationship, tailored for concrete, accurately anticipates the behavior of reinforced earth beams under bending. This suggests that the model has potential utility in designing steel-reinforced SE beams with an optimal reinforcement configuration to fulfill specific structural requirements. Moreover, the adoption of this model might address challenges related to limited understanding of the behavior of earthen materials and their interaction with steel reinforcement.

In conclusion, this study underscores the potential of projected steel-reinforced earthen materials. It also indicates that methodologies from existing RC structure models can be applied to reinforced SE structures, offering a potential avenue towards more sustainable and cost-efficient construction methodologies.

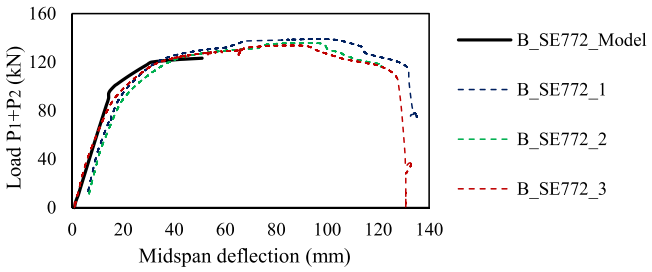

Fig. 15. Load P1 + P2 – midspan deflection relationship in comparison with B_SE772 model.

Declaration of Competing Interest

The authors declare that they have no known competing financial interests or personal relationships that could have appeared to influence the work reported in this paper.The authors declare that the present work has been realized in compliance with the Ethical Standards.

This study was funded by the aforementioned grant only.

Data Availability

Data will be made available on request.

Acknowledgments

Financial support from the HES-SO in the framework of the projects "NextEarthBuild – Une nouvelle génération d'éco-construction en terre d'excavation recycle – n° 98528" and "EcoAbri – Construction d'un abri t é moin en terre d'excavation et autres matériaux écologiques et indigènes en vue de la réalisation ultérieure d'un espace de rangement non chauffé – n° 108222" is gratefully acknowledged. Financial support from Innosuisse in the framework of the Project "Innosuisse – Shotearth: a sustainable excavated-soil based building material – n° 52127.1 IP-EE " is gratefully acknowledged as well. Financial support from the Italian Ministry of University and Research (MUR) in the framework of the projects PRIN 2022 "New eco-friendly building materials inspired by ancient constructions" (prot. 2022Y2RHHT; CUP E53D23003900006), FISA 2022-00183 "Earth-Tech") and "FAR Dipartimentale 2022–2023" (CUP: E93C22000590005 from University of Modena and Reggio Emilia are gratefully acknowledged. Luca Lanzoni is member of Gruppo Nazionale di Fisica Matematica (GNFM) of Istituto Nazionale di Alta Matematica (INdAM).

References

[1] Miccoli L, Müller U, Fontana P. Mechanical behaviour of earthen materials: A comparison between earth block masonry, rammed earth and cob. Constr Build Mater 2014;61:327–39. https://doi.org/10.1016/j.conbuildmat.2014.03.009.
[2] Morel JC, Mesbah A, Oggero M, Walker P. Building houses with local materials: means to drastically reduce the environmental impact of construction. Build Environ 2001;36:1119–26. https://doi.org/10.1016/S0360-1323(00)00054-8.
[3] Benhelal E, Zahedi G, Shamsaei E, Bahadori A. Global strategies and potentials to curb CO_2 emissions in cement industry. J Clean Prod 2013;51:142–61. https://doi.org/10.1016/j.jclepro.2012.10.049.
[4] Jaquin PA, Augarde CE, Gerrard CM. Chronological description of the spatial development of rammed earth techniques. Int J Archit Herit 2008;2:377–400. https://doi.org/10.1080/15583050801958826.
[5] Curto A, Lanzoni L, Tarantino AM, Viviani M. Shot-earth for sustainable constructions. Constr Build Mater 2020;239:117775.
[6] Franciosi M, Savino V, Lanzoni L, Tarantino AM, Viviani M. Changing the approach to sustainable constructions: An adaptive mix-design calibration process for earth composite materials. Compos Struct 2023:117143. https://doi.org/10.1016/j.compstruct.2023.117143.
[7] Vantadori, Żak S, Sadowski \Lukasz A, Ronchei C, Scorza D, Zanichelli A, et al. Microstructural, chemical and physical characterisation of the Shot-Earth 772. Constr Build Mater 2022;341:127766.
[8] A. D'Alessandro A. Meoni V. Savino M. Viviani F. Ubertini New self-sensing shot-earth cement-composites for smart and sustainable constructions: experimental validation on a full-scale vault Proc 6th Workshop N Bound Struct Concr 2022 Univ Salento - Acids Italy Chapter 2022.
[9] Tarantino AM, Cotana F, Viviani M, editors. Shot-Earth for an Eco-friendly and Human-Comfortable Construction Industry. Springer Nature Switzerland; 2023.
[10] Bacciocchi M, Savino V, Lanzoni L, Tarantino AM, Viviani M. Multi-phase homogenization procedure for estimating the mechanical properties of shot-earth materials. Compos Struct 2022;295:115799. https://doi.org/10.1016/j.compstruct.2022.115799.
[11] Minke G. Building with Earth: Design and Technology of a Sustainable Architecture. Walter. de Gruyter GmbH; 2021.
[12] Dobson S. Keynote papers Rammed earth in the modern world. Rammed Earth Construction. CRC Press; 2015.
[13] Savino V, Franciosi M, Viviani M. Engineering and analyses of a novel Catalan vault. Eng Fail Anal 2023;143:106841. https://doi.org/10.1016/j.engfailanal.2022.106841.
[14] Wardeh G, Ghorbel E, Gomart H, Fiorio B. Experimental and analytical study of bond behavior between recycled aggregate concrete and steel bars using a pullout test. Struct Concr 2017;18:811–25. https://doi.org/10.1002/suco.201600155.
[15] FIB-federation internationale du beton. CEB-FIP Model Code 1990: Design Code. Thomas Telford Ltd; 1993.
[16] FIB-federation internationale du beton. CEB-FIP Model Code for Concrete Structures 2010. Ernst & Sohn; 2013.
[17] Ciancio D., Beckett C. Rammed earth: an overview of a sustainable construction material 2013.
[18] Houben H, Guillaud H. Earth. Construction: A Comprehensive Guide. Reissue edizione. London: Practical Action Pub; 1994.
[19] CEN (European Committee for Standardization). Tests for geometrical properties of aggregates - Part 1. Determination of particle size distribution - Sieving method. Brussels, Belgium: CEN; 2012.
[20] SN-VSS. Identification des sols. Méthode de laboratoire avec classification selon l'USCS. Switzerland: Zürich; 1997.
[21] Bazant Z, Sener S. Size effect in pullout tests. Acids Mater J 1988;85:347–51.
[22] Bažant ZP. Size effect in blunt fracture: concrete, rock, metal. J Eng Mech 1984;110:518–35. https://doi.org/10.1061/(ASCE)0733-9399(1984)110:4(518).
[23] Padmanabham K, Rambabu K. Static pullout tests on retrofitted anchorage system in concrete using supplementary reinforcement. Saudi J Civ Eng 2022;6:79–94. https://doi.org/10.36348/sjce.2022.v06i04.004.
[24] Bayoumi E-S. Effect of hybrid fibers on bond strength of fiber reinforced concrete. ARPN J Eng Appl Sci 2020;15:2958–68.
[25] Freitas E, Louro AS, Costa H, Cavaco ES, Júlio E, Pipa M. Bond behaviour between steel / stainless-steel reinforcing bars and low binder concrete (LBC). Eng Struct 2020;221:111072. https://doi.org/10.1016/j.engstruct.2020.111072.
[26] CEN (European Committee for Standardization). Testing hardened concrete - Part 3: Compressive strength of test specimens. Brussels, Belgium: CEN,; 2003.
[27] Nawaz W., Elchalakani M., Karrech A., Australia W. Flexure Behaviour Of All Light Weight Reinforced Concrete Beams Externally Strengthened With CFRP Laminates n.d.
[28] Rydval M, Huňka P, Kolísko J. Dependence of Load Bearing Capacity on Homogeneity of Steel Fiber Distribution. Appl Mech Mater 2015;732:353–6.
[29] Lee HY, Jung WT, Chung W. Flexural strengthening of reinforced concrete beams with pre-stressed near surface mounted CFRP systems. Compos Struct 2017;163:1–12. https://doi.org/10.1016/j.compstruct.2016.12.044.
[30] Abdalla JA, Hawileh RA, Nawaz W, Mohammed A. Reinforced Concrete Beams Externally Strengthened in Flexure using Hybrid Systems. IEEE; 2018. p. 1–5.
[31] Godat A, L'Hady A, Chaallal O, Neale KW. Bond behavior of the ETS FRP bar shear-strengthening method. J Compos Constr 2012;16:529–39. https://doi.org/10.1061/(ASCE)CC.1943-5614.0000280.
[32] Swiss Society of Engineers and Architects. Swiss Standard SIA 262:2013: Concrete Structure. 2013.
[33] Khadka B, Shakya M. Comparative compressive strength of stabilized and unstabilized rammed earth. Mater Struct 2016;49:3945–55. https://doi.org/10.1617/s11527-015-0765-5.